Acta Pharmaceutica Sinica B 2024;14(10):4493−4508

Chinese Pharmaceutical Association
Institute of Materia Medica, Chinese Academy of Medical Sciences

Acta Pharmaceutica Sinica B

www.elsevier.com/locate/apsb
www.sciencedirect.com

ORIGINAL ARTICLE

Zinc oxide nanoparticles with catalase-like nanozyme activity and near-infrared light response: A combination of effective photodynamic therapy, autophagy, ferroptosis, and antitumor immunity

Jingru Wang [a,b], Man Liu [a,b], Jingwen Wang [a,b], Zhuoyue Li [a,b], Zhenhan Feng [a,b], Meiqi Xu [a,b], Hui Wang [a,b], Hui Li [a,b], Zhantao Li [a,b], Jianming Yu [a,b], Junwei Liu [a,b], Qingchao Wei [a,b], Shuang Zhang [c,*], Xuan Zhang [a,b,d,*]

[a]*Department of Pharmaceutics, School of Pharmaceutical Sciences, Peking University, Beijing 100191, China*
[b]*Beijing Key Laboratory of Molecular Pharmaceutics and New Drug Delivery Systems School of Pharmaceutical Sciences, Peking University, Beijing 100191, China*
[c]*School of Pharmaceutical Sciences, Capital Medical University, Beijing 100069, China*
[d]*Ningbo Institute of Marine Medicine, Peking University, Ningbo 315832, China*

Received 21 April 2024; received in revised form 18 June 2024; accepted 20 June 2024

KEY WORDS

Photodynamic therapy;
Near-infrared light;
Tissue penetration;
Catalase-like nanozyme;
Ferroptosis;
Autophagy;
Immunity;
Zinc oxide nanoparticles

Abstract We prepared biocompatible and environment-friendly zinc oxide nanoparticles (ZnO NPs) with upconversion properties and catalase-like nanozyme activity. Photodynamic therapy (PDT) application is severely limited by the poor penetration of UV−Visible light and a hypoxic tumor environment. Here, we used ZnO NPs as a carrier for the photosensitizer chlorin e6 (Ce6) to construct zinc oxide −chlorin e6 nanoparticles (ZnO-Ce6 NPs), simultaneously addressing both problems. In terms of penetration, ZnO NPs convert 808 nm near-infrared light into 401 nm visible light to excite Ce6, achieving deep-penetrating photodynamic therapy under long-wavelength light. Interestingly, the ability to emit short-wavelength light under long-wavelength light is usually observed in upconversion nanoparticles. As nanozymes, ZnO NPs can catalyze the decomposition of hydrogen peroxide in tumors, providing oxygen for photodynamic action and relieving hypoxia. The enhanced photodynamic action produces a

*Corresponding authors.
E-mail addresses: zshuang@ccmu.edu.cn (Shuang Zhang), xuanzhang@bjmu.edu.cn (Xuan Zhang).

Peer review under the responsibility of Chinese Pharmaceutical Association and Institute of Materia Medica, Chinese Academy of Medical Sciences.

https://doi.org/10.1016/j.apsb.2024.07.002

large amount of reactive oxygen species, which overactivate autophagy and trigger immunogenic cell death (ICD), leading to antitumor immunotherapy. In addition, even in the absence of light, ZnO and ZnO-Ce6 NPs can induce ferroptosis of tumor cells and exert antitumor effects.

1. Introduction

Although metals constitute only 2.5% of human body mass, they play important roles in many biological processes[1]. With the development of nanomaterials and drug delivery systems, metal-based antitumor nanomedicines have been developed for cancer diagnosis and treatment. For example, gold nanoparticles act as radiosensitizers during radiation therapy, thereby increasing cancer cell sensitivity to X-rays[2]. However, some nanomedicines contain non-physiological exogenous metals that are inherently toxic at therapeutic doses (such as platinum and gold) [3,4]. Zinc is an essential trace element in the human body owing to its unique functions[5]. Zinc oxide nanoparticles (ZnO NPs), which are biocompatible, chemically stable, and environment-friendly, are potential materials for biomedical applications. ZnO NP is a promising material for photonic applications in the ultraviolet or blue spectral range owing to its large bandgap, and its high exciton binding energy enables efficient exciton emission[6]. Interestingly, it emits 401 nm visible light under 808 nm near-infrared (NIR) light. Therefore, ZnO NPs have the potential to replace 401 nm visible NIR light with 808 nm light, resulting in significant tissue penetration. This property is similar to that of upconversion nanoparticles (UCNPs), but ZnO NPs are safer, healthier, and easier to obtain than lanthanide ion-doped UCNPs[7,8].

The advantages of low cost, preparation ease, and high stability have led to the development of various nanozymes (artificial enzymes based on nanomaterials) with intrinsic enzyme-like properties for drug delivery[11], including metals, metal oxides, and metal nanocomposites[9,10]. As reported in a previous study, ZnO NPs promote H_2O_2 decomposition to produce oxygen[12]; thus, they can be regarded as catalase-like nanozymes and used to design the nano-platform for overcoming hypoxia in tumors.

Photodynamic therapy (PDT) is a clinically recognized treatment[13-15] with spatial selectivity, low invasiveness, good dose reproducibility, and lower systemic toxicity than chemotherapy and radiotherapy[16,17]. The anticancer principle of PDT is that the photosensitizer (PS) is usually activated under specific light and transfers energy to the surrounding oxygen to generate reactive oxygen species (ROS), leading to cancer cell necrosis or apoptosis[18-20]. Besides, ROS are important triggers of autophagy[21,22], which is generally considered a cytoprotective response that plays a crucial role in cell survival[23]. However, the overactivation of autophagy can cause autophagic cell death[24], and ROS overproduction should convert autophagy from pro-survival to pro-death, thus contributing to antitumor effects. PDT also induces immunogenic cell death (ICD), triggers dendritic cell (DC) maturation, and ultimately increases the T cell activation, proliferation, and infiltration to achieve a systemic immune response for antitumor immunotherapy[25,26].

Several issues limit the efficacy of PDT, including its limited penetration depth in deep-seated tumors[13,27]. The excitation wavelength used in PDT is usually in the visible light range, and the penetration depth of light is limited from a few millimeters to a few centimeters[28]. To penetrate the tissues deeply, the optical window that facilitates light penetration should be within the NIR range[29]. Two-photon NIR excitation[30,31] and UCNP are commonly used techniques[32,33]. However, two-photon NIR excitation requires short-pulse femtosecond NIR lasers, which may not be available in most laboratories or hospitals, and UCNPs consisting of rare-earth elements are usually complicated to prepare and toxic[34]. The lack of endogenous oxygen in tumors is another limitation, as PDT is a highly oxygen-dependent procedure that aggravates tumor hypoxia, which in turn reduces PDT efficacy[35]. Two common solutions are using suitable oxygen carriers (such as hemoglobin[36] or perfluorocarbons[37,38]) to deliver oxygen directly to tumors and generate oxygen *in situ* within the tumor. Many catalase- or MnO_2-containing nanoplatforms have been designed to transform endogenous H_2O_2 into oxygen[39,40]. Notably, ZnO NPs with upconversion properties and catalase-like nanozyme activity should address both problems simultaneously. In addition, ZnO NPs can disrupt iron homeostasis to induce ferroptosis in tumor cells[41].

Therefore, we developed zinc oxide-chlorin e6 nanoparticles (ZnO-Ce6 NPs) comprising ZnO NP nanozymes and Ce6, which can be excited by 808 nm NIR light for deep tissue penetration and generate oxygen to overcome the limitations of PDT (Fig. 1). In our study, the 808 nm laser irradiated-ZnO-Ce6 NPs emitted visible light at 401 nm (from ZnO NPs) to stimulate the loaded Ce6 and cause photodynamic action. In addition, ZnO-Ce6 NPs can promote H_2O_2 decomposition to produce oxygen *via* ZnO NP nanozymes, providing sufficient oxygen for PDT, relieving hypoxia, and normalizing the blood vessels in tumors. Benefiting from deep penetration and oxygen supply, 808 nm laser irradiated-ZnO-Ce6 NPs generated large amounts of ROS and excessively activated autophagy, contributing to autophagic tumor cell death. In contrast, even in the absence of light, ZnO-Ce6 NPs induced cell death *via* ferroptosis. ICD with an enhanced damage-associated molecular pattern (DAMP) release was elicited, promoting DC maturation and subsequently activating T lymphocytes and natural killer (NK) cells. Consequently, ZnO-Ce6 NP-mediated PDT elicited effective antitumor activity, inhibited tumor growth, and ablated some tumors.

2. Materials and methods

2.1. Materials

Chlorin e6 was obtained from Frontier Scientific, Inc. (Logan, UT, USA). Zinc acetate dehydrate ($Zn(OAc)_2 \cdot 2H_2O$) was purchased from Energy Chemical (Shanghai, China). 30% hydrogen peroxide solution was purchased from Beijing Chemical Co., Ltd. (Beijing, China). Singlet oxygen sensor green (SOSG) reagent and

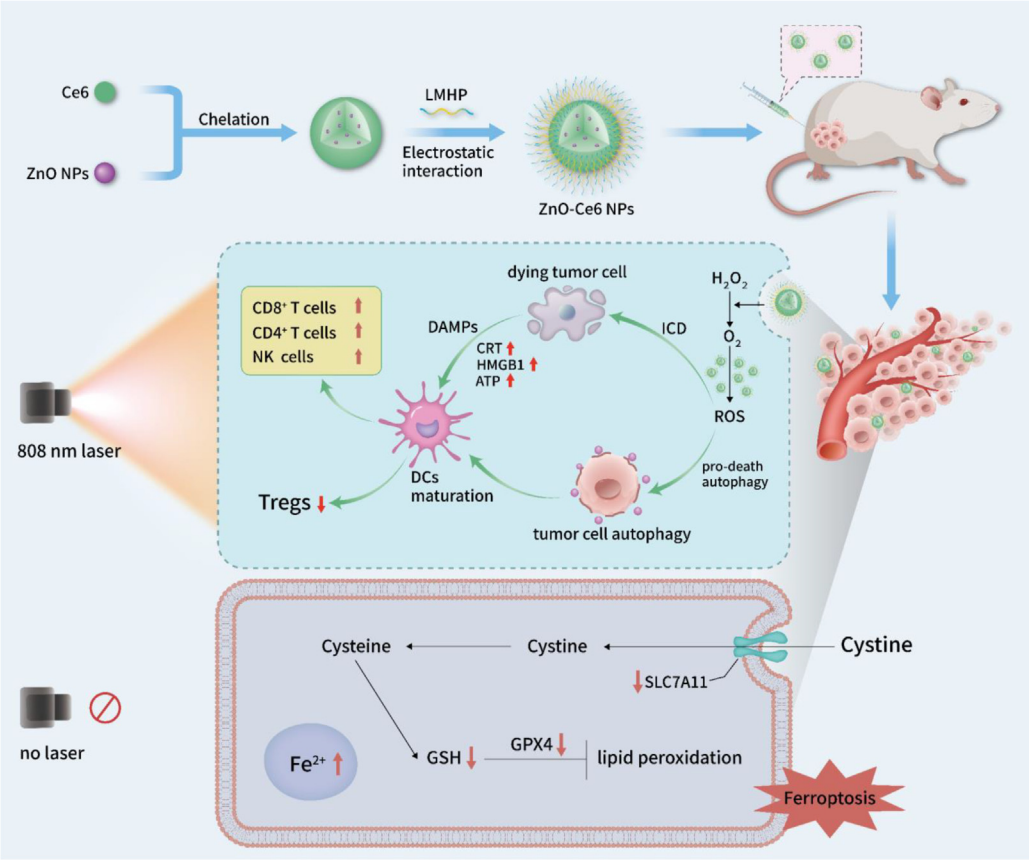

Figure 1 The illustration of the antitumor effect of ZnO-Ce6 NPs. Owing to the deep penetration and oxygen supply under 808 nm laser irradiation, the ZnO-Ce6 NPs enhanced PDT efficiency, excessively activating pro-death autophagy and contributing to immunogenic cell death (ICD) and systemic immunity. Even in the absence of laser, ZnO-Ce6 NPs cause iron overload; downregulate solute carrier family 7 member 11 (SLC7A11), glutathione (GSH), and glutathione peroxidase 4 (GPX4) levels; and boost lipid peroxidation, ultimately leading to the ferroptosis of tumor cells.

2′,7′-dichlorodihydrofluorescein diacetate (DCFH-DA) were from Dalian Meilun Biotechnology Co., Ltd. (Dalian, China). The anti-CD11c FITC, anti-CD86 APC, and anti-MHCII PE were obtained from Biolegend (San Diego, CA, USA). The anti-CD16/CD32 antibody was from Elabscience Biotechnology Co., Ltd. (Wuhan, China). The anti-CD3e PE, anti-Foxp3 PE-cy5, anti-CD4 FITC, anti-CD8a APC-eFluor780, and anti-CD49b APC antibodies were from eBioscience (San Diego, CA, USA). The primary anti-HIF-1α antibody and anti-calreticulin antibody were purchased from Bioss (Beijing, China). The anti-LC3B and anti-p62 antibodies were from ABclonal (Wuhan, China).

The murine breast cancer 4T1 cell line was purchased from the Cell Resource Center (Beijing, China). Cells were cultured by cell culture medium from M&C Gene Biotech Co., Ltd. (Beijing, China) and fetal bovine serum (FBS) from GIBCO (Carlsbad, CA, USA) in accordance with the recommended conditions of ATCC.

Female BALB/c mice (6 weeks) were provided by the Experimental Animal Center of Peking University Health Science Center. All of the animal experiments adhered to the principles of care and use of laboratory animals and were approved by the Peking University Biomedical Ethics Committee (approval number: LA2021343).

2.2. *Preparation and characterization of ZnO-Ce6 NPs*

ZnO NPs were prepared using a sol−gel method[42−44]. $Zn(OAc)_2 \cdot 2H_2O$ was dissolved in hot ethanol and stirred for 2 h until completely dissolved. Similarly, NaOH was added to the hot ethanol and stirred for 2 h. The NaOH ethanol solution was then passed through a 0.22-μm micropore filter and added dropwise to the $Zn(OAc)_2 \cdot 2H_2O$ ethanol solution under rapid stirring, reacting in an ice bath for 4 h to obtain ZnO NPs. Ce6 ethanol solution was added to the ZnO NPs ethanol solution under stirring. The mixture was stirred for 2 min and then separated by centrifugation. The precipitate was resuspended in 300 μL of DMSO. The low-molecular-weight heparin (LMHP)[45] water solution was added to the precipitate DMSO resuspension solution under stirring. The mixture was then placed in a 37 °C gas bath shaker for 4 h and added dropwise to water under stirring to obtain ZnO-Ce6 NPs.

The size distribution and zeta potential of ZnO-Ce6 NPs were measured using a dynamic light scattering detector (Malvern, Nano-ZS, Worcestershire, UK). Morphology characterization was conducted using a transmission electron microscope (JEOL, JEM-2100, Tokyo, Japan) operating at a voltage of 200 kV. UV−Visible (UV−Vis) absorption spectra were recorded on a UV−Vis spectrophotometer (Shimadzu, UV-2600, Kyoto, Japan). Fourier transform infrared spectra were obtained using a Fourier transform infrared spectrometer (Thermo Fisher, Nicolet-6700, Waltham, MA, USA). Fluorescence spectra of Ce6 were obtained using a fluorescence spectrophotometer (Shimadzu, RF-5301PC, Kyoto, Japan). Fluorescence spectra of ZnO NPs and ZnO-Ce6 NPs were measured using an infrared fluorescence spectrometer (HORIBA Jobin Yvon, Nanolog FL3-2Ihr, Paris, France).

2.3. In vitro photodynamic action

Oxygen generation was quantified using a dissolved oxygen analyzer (HANNA, HI2400, Padua, Italy). The following experimental groups were tested for oxygen generation after saturation with sufficient nitrogen and sealing with oil: (1) H_2O_2 irradiated with an 808 nm laser or left untreated; (2) mixture of H_2O_2 and ZnO NPs irradiated with an 808 nm laser or a 660 nm laser, or left untreated; (3) mixture of H_2O_2 and ZnO-Ce6 NPs irradiated with an 808 nm laser or left untreated.

The generation of ROS was assessed using a fluorescent ROS probe, DCFH. The probe was mixed with ZnO NPs, Ce6, or ZnO-Ce6 NPs and subjected to laser irradiation (0.5 W/cm^2) at 808 or 660 nm. The fluorescence intensity was measured at 0, 5, 10, 15, 20, and 25 min to evaluate the ROS levels.

For penetration evaluation, the Ce6 group was irradiated with a 660 nm laser (0.5 W/cm^2), and the ZnO-Ce6 NPs group was irradiated with an 808 nm laser (0.5 W/cm^2), with or without being blocked by 1 cm thick pig muscle tissue. Fluorescence intensity was measured at 0, 10, 20, and 30 min. The percentage of ROS reduction was calculated using Eq. (1):

$$\text{ROS reduction percentage (\%)} = (\text{Fluorescence intensity when unblocked} - \text{Fluorescence intensity when blocked}) / \text{Fluorescence intensity when unblocked} \times 100 \quad (1)$$

Singlet oxygen generation was measured using the SOSG probe. ZnO-Ce6 NPs (Ce6 concentration: 50 μmol/L) were mixed with SOSG (2 μmol/L) and subjected to laser irradiation (0.5 W/cm^2) at 808 nm. The mixture was saturated with sufficient nitrogen in hypoxic groups.

Intracellular ROS generation was assessed using a fluorescent ROS probe, DCFH-DA. 4T1 cells were loaded with DCFH-DA in confocal dishes for 30 min, followed by three washes. The cells were then treated with ZnO NPs, Ce6, or ZnO-Ce6 NPs and irradiated with an 808 or 660 nm laser for 15 min. After incubating for 2 h, the cells were stained with Hoechst 33342 and examined under a confocal laser scanning microscope.

To evaluate intracellular ROS generation under hypoxic (1% O_2) conditions, 4T1 cells were plated on confocal dishes and incubated for 12 h, followed by exposure to hypoxic (1% O_2) conditions for an additional 12 h. Subsequently, cells were subjected to similar treatments under hypoxic (1% O_2) conditions and then observed.

To detect the HIF-1α protein in 4T1 cells, the cells were plated on confocal dishes and incubated for 12 h, followed by exposure to hypoxic conditions (1% O_2) for an additional 12 h. After various treatments, the cells were maintained under hypoxic conditions (1% O_2) for 4 h. Subsequently, the cells were fixed, permeabilized, and treated with the blocking buffer. The primary anti-HIF-1α antibody (Bioss, Beijing, China), followed by the secondary Alexa Fluor488-conjugated goat anti-rabbit IgG antibody (Bioss, Beijing, China) and Hoechst 33342, were added sequentially. The cells were then visualized using confocal laser scanning microscopy (CLSM, Leica, TCS-SP8 STED 3X, Wetzlar, Germany).

2.4. In vitro detection of autophagy

To detect LC3 and p62 in 4T1 cells, cells were plated on confocal dishes and divided into experimental groups for treatment lasting 24 h. After treatment, the cells were fixed, permeabilized, and treated with the blocking buffer. Subsequently, the primary anti-LC3B antibody (ABclonal, Wuhan, China) or the primary anti-p62 antibody (ABclonal, Wuhan, China), followed by the secondary Alexa Fluor488-conjugated goat anti-rabbit IgG antibody and Hoechst 33342, were added sequentially. The cells were then visualized using confocal laser scanning microscopy.

2.5. In vitro assessment of ICD markers

Surface exposure of calreticulin (CRT) was assessed using flow cytometry and confocal immunofluorescence. For confocal immunofluorescence analysis, 4T1 cells were seeded onto dishes and cultured overnight. Following various treatments and an additional 6 h incubation period, cells were treated with blocking buffer, anti-calreticulin antibody (Bioss, Beijing, China), Alexa Fluor 488-conjugated secondary antibody, and Hoechst 33342 sequentially. Subsequently, cells were visualized using CLSM (Leica). In flow cytometry, after various treatments and an additional 6 h incubation period, cells were harvested and incubated sequentially with anti-CRT antibody and Alexa Fluor 488-conjugated secondary antibody. Flow cytometry analysis was then conducted on the cells.

Extracellularly released high mobility group box 1 (HMGB1) and adenosine triphosphate (ATP) were detected using the HMGB1 ELISA Kit (CUSABIO, Wuhan, China) and the chemiluminescence ATP assay kit (Beyotime, Shanghai, China), respectively, following the manufacturer's instructions.

2.6. In vitro induction of DC maturation

Bone marrow-derived dendritic cells (BM-DCs) were generated from 6-week-old female BALB/c mice[46]. The femurs and tibiae of the mice were isolated, and muscle tissue was removed. The bone marrow was washed with RPMI 1640, and red blood cells were lysed. The resulting mononuclear cell pellet was collected and mixed with 10 mL of Iscove-modified Dulbecco's medium (IMDM) containing 10% FBS, 100 units/mL penicillin, 100 mg/mL streptomycin, 20 ng/mL recombinant mouse GM-CSF (GenScript, Piscataway, NJ, USA), 20 ng/mL recombinant mouse IL-4 (GenScript, Piscataway, NJ, USA), and 50 μmol/L β-mercaptoethanol (Sigma, Saint Louis, MO, USA) in a 100 mm bacterial culture dish on Day 0. On Day 3, an additional 10 mL of IMDM medium was added to the culture dish. On Days 6 and 8, half of the culture supernatant was collected and centrifuged, and the cell pellet was resuspended in 10 mL of fresh IMDM medium and returned to the original plate. BM-DCs were obtained on Day 10.

4T1 cells were seeded in 12-well plates and incubated overnight. In the Ce6 group, the cells were treated with Ce6 (5 μg/mL) under 660 nm laser irradiation for 15 min (0.5 W/cm^2). In the ZnO-Ce6 NPs + L (808 nm) group, the cells were treated with ZnO-Ce6 NPs (Ce6 concentration: 5 μg/mL) under 808 nm laser irradiation for 15 min (0.5 W/cm^2). After another 12 h of incubation, the supernatant of the 4T1 cells was collected. Additionally, BM-DCs were seeded in 12-well plates and incubated overnight. Then, the original medium of BM-DCs was discarded, and the cell supernatant of the 4T1 cells was added to the corresponding wells of BM-DCs. Following an additional 24 h incubation, BM-DCs were collected and stained.

The collected BM-DCs from the aforementioned groups were first incubated with the blocking buffer for 1 h, followed by incubation with monoclonal antibodies (mAbs), including anti-

CD11c FITC, anti-CD86 APC and anti-MHCII PE (Biolegend, San Diego, CA, USA) for 2 h. Finally, BM-DCs were analyzed using flow cytometry (Gallios, Beckman Coulter, Brea, CA, USA).

2.7. *In vivo antitumor activity*

All animal experiments were conducted in compliance with the principles of care and use of laboratory animals and were approved by the Peking University Biomedical Ethics Committee (approval number: LA2021343).

6-week-old female BALB/c mice were subcutaneously injected with 1×10^6 4T1 cells to establish 4T1 tumor models. Once tumors reached approximately 100 mm^3, the 4T1 tumor-bearing mice were randomly divided into 6 groups ($n = 5$). In the control group, mice received no treatment. In the Ce6 group, mice were treated with Ce6 alone. In the Ce6+L (808 nm) group, mice were injected with Ce6 and irradiated with an 808 nm laser. In the Ce6+L (660 nm) group, mice were injected with Ce6 and irradiated with a 660 nm laser. In the ZnO-Ce6 NPs group, mice were treated with ZnO-Ce6 NPs. In the ZnO-Ce6 NPs + L (808 nm) group, mice were treated with ZnO-Ce6 NPs and irradiated with an 808 nm laser. All formulations were administered *via* intratumoral injection with an equal Ce6 dose of 2 mg/kg, and laser irradiation was performed at 1 W/cm^2 for 15 min. Mice were treated every 3 days, totaling 4 times. Tumor volume was measured every two days using digital calipers and calculated using Eq. (2):

$$V = L \times S \times S/2 \quad (2)$$

where L represents the longest dimension and S represents the shortest dimension.

To assess ROS generation *in vivo*, 4T1 tumor-bearing mice with tumors approximately 100 mm^3 in volume were divided into 3 groups. The intratumoral injection dose was fixed at a relative Ce6 dose of 2 mg/kg. After 2 h, 50 μL of DCFH-DA solution (40 μmol/L) was injected intratumorally into the mice, followed by laser irradiation (1 W/cm^2) for 15 min, administered 30 min later. Subsequently, the mice were sacrificed, and the tumors from each group were collected and cryosectioned onto slides ($n = 3$). The sections were fixed and stained with Hoechst 33342. Visualization was performed using CLSM (Leica, TCS-SP8, Wetzlar, Germany).

To evaluate the alleviation of the tumor hypoxic microenvironment, 4T1 tumor-bearing mice with tumors approximately 100 mm^3 in volume were divided into 4 groups. The intratumoral injection dose was fixed at a relative Ce6 dose of 2 mg/kg, followed by 15 min of laser irradiation (1 W/cm^2) for each group. After 4 h, the mice were sacrificed, and the tumors from each group were collected and cryosectioned onto slides ($n = 3$). Cryostat sections of the tumors were prepared and stained. In brief, the sections were fixed and permeabilized, followed by treatment with blocking buffer, primary anti-HIF-1α antibody, anti-CD31-APC (eBioscience, San Diego, CA, USA), secondary Alexa Fluor488-conjugated goat anti-rabbit IgG antibody, and Hoechst 33342, successively. The sections were then visualized using CLSM (Leica).

For *in vivo* assessment of antitumor immunity, quantitative analysis of DCs and T cells was conducted using flow cytometry. Tumors, spleens, and tumor-draining lymph nodes were collected for evaluation 2 days after the last administration. Tumor-draining lymph nodes were ground with glass slides, while tumors and spleens were cut into small pieces and digested using a mixture of 1500 U/mL collagenase, 1000 U/mL hyaluronidase, and DNase at 37 °C. The tissue suspension was filtered through a nylon mesh filter to obtain a single-cell suspension. The single-cell suspension from tumors was purified using the mouse tumor infiltrating tissue lymphocyte isolation kit, followed by the harvesting of lymphocytes. The single-cell suspension of spleens was lysed with red blood cell lysis buffer and filtered through nylon mesh filters (70 μm). The harvested cells were then incubated with Fc blocking antibody (anti-CD16/CD32) followed by staining with anti-CD11c FITC, anti-CD86 APC, and anti-MHCII PE antibodies for DC maturation analysis and with anti-CD3e PE, anti-Foxp3 PE-cy5, anti-CD4 FITC, anti-CD8a APC-eFluor780, and anti-CD49b APC antibodies for T cell and NK cell analysis. Finally, the samples were analyzed by flow cytometry.

3. Results and discussion

3.1. *ZnO-Ce6 NP preparation and characterization*

The PS Ce6 is primarily excited at 660 nm in PDT[47,48]. We used ZnO NPs to prepare the ZnO-Ce6 NPs to excite Ce6 with 808 nm NIR light and hoped that they responded to 808 nm NIR light to induce the photodynamic action.

The ZnO NPs and Ce6 were bound by chelation (Fig. 2A). The interaction between ZnO NPs and Ce6 was measured by MicroScale Thermophoresis (MST) and belonged to the chemical bond level, consistent with chelation (Fig. 2B). And then the negatively charged LMHP was bound by electrostatic interactions (Fig. 2A). LMHP is a fragment obtained by enzymatic or chemical degradation of heparin. Compared with ordinary heparin, LMHP retains the polysaccharide structure of heparin, but it has a lower bleeding risk. LMHP contains sulfate and carboxyl groups, so it is negatively charged[49] and can form nanoparticles with other substances through chemical modification or electrostatic adsorption for the delivery of antitumor drugs, proteins, and genes[50,51]. When LMHP is used as a nanocarrier material, it has good biocompatibility, low toxicity, easy chemical modification, and is easy to obtain. The nanoparticles protected by LMHP also have a long-term cycling effect *in vivo*[52]. Besides, LMHP can also inhibit tumor angiogenesis, inhibit the proliferation of tumor cells, and induce apoptosis[53,54]. The particle size and zeta potential of ZnO-Ce6 NPs were 44.67 ± 1.29 nm and-20.00 ± 1.41 mV, respectively (Fig. 2C and D). The weight percent of Ce6 in ZnO-Ce6 NPs was 12.01 % (*w*/*w*). Transmission electron microscopy (TEM) images indicated the spherical shape and uniform size of the ZnO-Ce6 NPs (Fig. 2E). The UV−Vis absorption peaks of ZnO-Ce6 NPs were at approximately 350, 400, and 650 nm (Fig. 2F), which were also observed in the UV−Vis spectra of the ZnO NPs and Ce6. The Fourier transform infrared (FTIR) spectrum results indicated that the LMHP bound to the ZnO-Ce6 NP surface (Supporting Information Fig. S1).

The fluorescence excitation peak for Ce6 was observed at 404 nm (Fig. 2G). Interestingly, the emission peak for ZnO NPs excited by 808 nm light was at 401 nm, which overlapped with the excitation peak of Ce6 (404 nm), indicating that this 401 nm emission peak of ZnO NPs could be employed to excite Ce6 to induce photodynamic action. The emission peak of the ZnO-Ce6 NPs excited by 808 nm light at 401 nm was partially quenched by Ce6, with potential energy transfer from the ZnO NPs to the decorated Ce6 (Fig. 2G). The emission peak of ZnO-Ce6 NPs

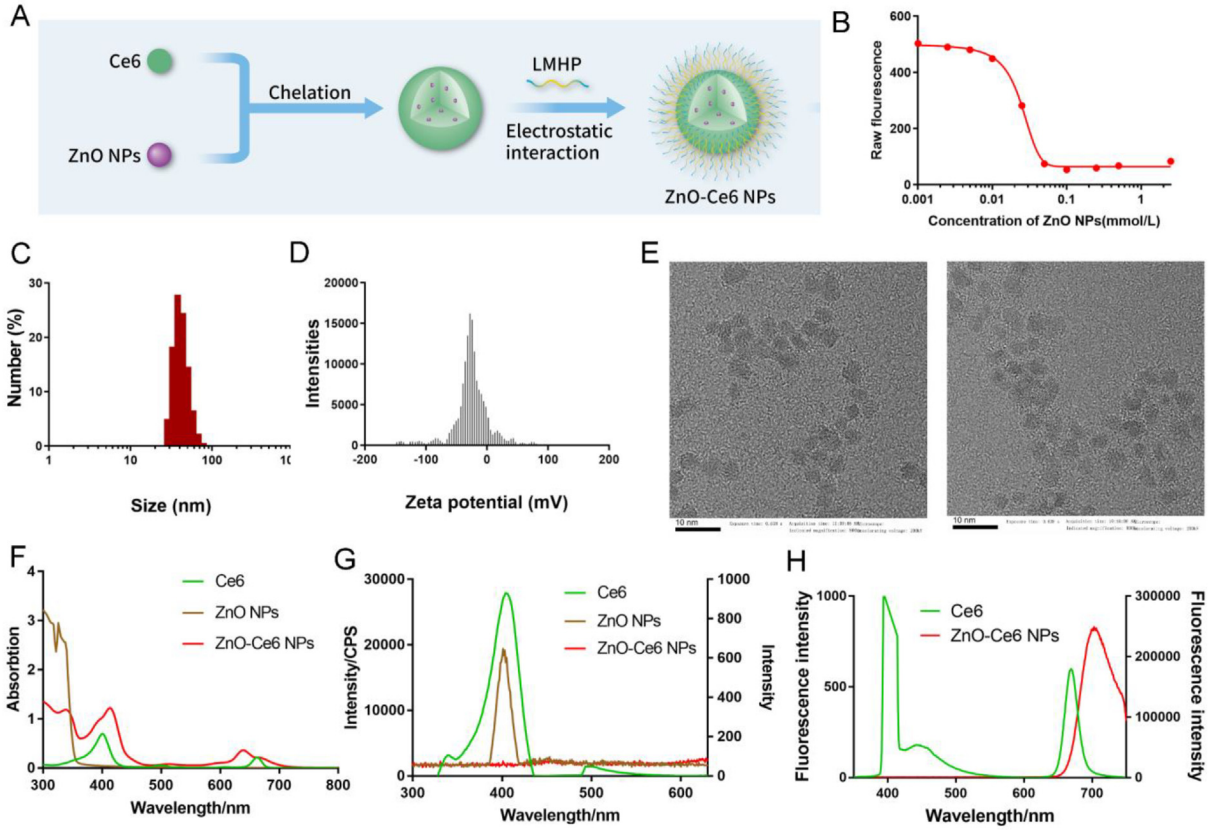

Figure 2 Zinc oxide−chlorin e6 nanoparticle (ZnO-Ce6 NP) preparation and characterization; (A) ZnO-Ce6 NP preparation; (B) Compare Hill-Fit by MST; (C) Size distribution of ZnO-Ce6 NPs measured by dynamic light scattering (DLS); (D) Zeta potential of ZnO-Ce6 NPs; (E) Transmission electron microscopy (TEM) image of ZnO NPs (left) and ZnO-Ce6 NPs (right), scale bar = 10 nm; (F) UV−Vis absorption spectra of ZnO-Ce6 NPs, ZnO NPs, and Ce6; (G) Fluorescence excitation spectrum of Ce6 (emission wavelength: 675 nm) and fluorescence emission spectra of ZnO and ZnO-Ce6 NPs (excitation wavelength: 808 nm); (H) Fluorescence emission spectrum of Ce6 (excitation wavelength: 401 nm) and fluorescence emission spectra of ZnO-Ce6 NPs (excitation wavelength: 808 nm).

excited by 808 nm light, at approximately 700 nm, was similar to that of Ce6 excited by 401 nm light, indicating that the Ce6 existing in the ZnO-Ce6 NPs was successfully excited (Fig. 2H).

The results indicated that the upconversion functional ZnO NPs could convert 808 nm NIR light to 401 nm light for further excitation of Ce6 decorated on the ZnO NP surface to induce photodynamic action.

3.2. *Enhanced photodynamic action of ZnO-Ce6 NPs in vitro*

Upon exposure to specific laser irradiation, the PS can be promoted to an excited triplet state and transfer energy to the surrounding oxygen to generate ROS, which causes photodynamic action[55,56]. Therefore, this oxygen-dependent photodynamic process consumes a large amount of oxygen to maintain effective PDT. However, tumor tissues generally suffer from severe hypoxia, which is aggravated by this photodynamic process, in turn reducing PDT efficacy[57,58]. Tumors contain a high amount of hydrogen peroxide (H_2O_2) [59,60]. Moreover, ZnO NPs catalyze H_2O_2 decomposition, generating oxygen[12,61,62], which could be regarded as nanozymes with peroxidase−mimic activity. Therefore, we suggest that oxygen generation *via* ZnO NP nanozymes can supply oxygen for PDT and overcome tumor hypoxia.

The ZnO NPs significantly produced oxygen when incubated with H_2O_2 (Fig. 3A). Moreover, ZnO-Ce6 NPs significantly produced oxygen when incubated with H_2O_2, indicating that ZnO-Ce6 NPs can also generate oxygen *via* ZnO NP nanozymes in the presence of H_2O_2. However, the oxygen produced by the 808 nm laser irradiated-ZnO-Ce6 NPs when incubated with H_2O_2 significantly decreased, which may be because these NPs would consume oxygen due to photodynamic action. Thus, the 808 nm laser irradiated-ZnO-Ce6 NPs produced sufficient oxygen for further photodynamic action consumption.

In addition, the amount of oxygen produced by ZnO NPs when incubated with H_2O_2 was independent of laser irradiation (without laser irradiation, under 660 or 808 nm laser irradiation; Supporting Information Fig. S2).

The 808 nm laser irradiated-ZnO-Ce6 NPs produced ROS, confirming that Ce6 in ZnO-Ce6 NPs could likewise be excited by 808 nm light to produce ROS (Fig. 3B). At 25 min, ROS levels after 808 nm laser irradiated-ZnO-Ce6 NP treatment were considerably higher than those after 660 nm laser irradiated-Ce6 treatment. In addition, almost no ROS was produced after Ce6, 808 nm laser irradiated-Ce6, ZnO NP, and 808 nm laser irradiated-ZnO NP treatments (Fig. 3B and Supporting Information Fig. S3).

To investigate the deep tissue penetration of 808 nm laser irradiated-ZnO-Ce6 NPs, ROS generation was measured before and after 1 cm of pig muscle tissue blocked the laser, and the ROS loss percentage was calculated. The ROS loss percentage after 808 nm laser irradiated-ZnO-Ce6 treatment (50%) was

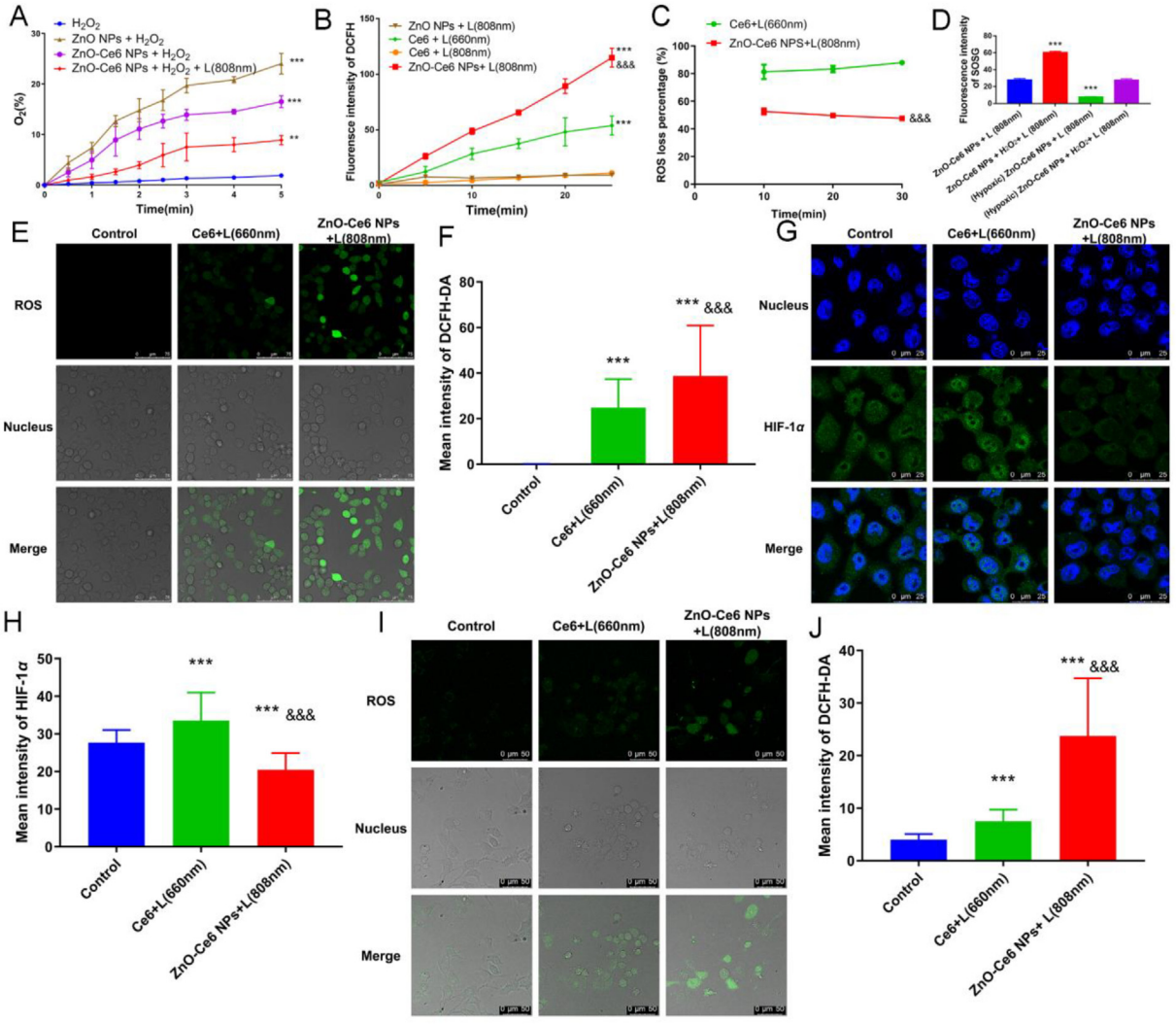

Figure 3 *In vitro* photodynamic therapy (PDT) performance. (A) Change of dissolved oxygen percentage over time when different samples were incubated with H_2O_2. Data are presented as mean ± SD ($n = 3$). $^{**}P < 0.01$ and $^{***}P < 0.001$ compared with H_2O_2 treatment; (B) Change in DCFH fluorescence upon irradiation time for different treatments; (C) Reduction percentage of DCFH-DA fluorescence intensity after 1 cm pig muscle tissue blocked the laser; (D) Singlet oxygen sensor green (SOSG) fluorescence after treatment with 808 nm laser irradiated-ZnO-Ce6 NPs under different conditions (with or without H_2O_2, normoxic or hypoxic); (E) Reactive oxygen species (ROS) signals in normoxic condition (scale bar = 75 μm) and (F) semi-quantitative analysis; (G) Hypoxia-induced factor 1α (HIF-1α) signals in hypoxic condition (scale bar = 25 μm) and (H) semi-quantitative analysis; (I) ROS signals in 4T1 cells in hypoxic condition (scale bar = 50 μm) and (J) Semi-quantitative analysis. (B−J) $^{***}P < 0.001$ compared with control group; $^{\&\&\&}P < 0.001$ compared with 660 nm laser irradiated-Ce6 treatment. Data are presented as mean ± SD ($n = 3$).

significantly lower than that after 660 nm laser irradiated-Ce6 treatment (84%), indicating a strong deep tissue penetration by 808 nm laser irradiated-ZnO-Ce6 NPs.

To further verify the oxygen generation function and oxygen-boosted PDT performance of ZnO-Ce6 NPs, a singlet oxygen sensor green (SOSG) was used as a singlet oxygen ($^1O_2$) probe to measure $^1O_2$ generation. The 808 nm laser irradiated-ZnO-Ce6 NPs generate $^1O_2$ (Fig. 3D), which greatly increased in the presence of H_2O_2, indicating that the oxygen produced by 808 nm laser irradiated-ZnO-Ce6 NPs in the presence of H_2O_2 could be supplied to boost PDT. Under hypoxic conditions, the $^1O_2$ generated by the 808 nm laser irradiated-ZnO-Ce6 NPs greatly decreased. However, when H_2O_2 was added, the generated $^1O_2$ almost reached the level of that of the 808 nm laser irradiated-ZnO-Ce6 NPs. These results indicate that the oxygen produced by 808 nm laser irradiated-ZnO-Ce6 NPs in the presence of H_2O_2 can be further used to generate $^1O_2$ and boost PDT.

Although ZnO NP nanozymes with peroxidase−mimic activity could produce oxygen in the presence of H_2O_2, they generated a trace amount of $^1O_2$ (Supporting Information Fig. S4).

The intracellular ROS generation function of ZnO-Ce6 NPs was also studied using CLSM. The ROS generation by 808 nm laser irradiated-ZnO-Ce6 NPs increased significantly (Fig. 3E and F), confirming that Ce6 in the ZnO-Ce6 NPs was excited by the 808 nm laser to produce ROS in 4T1 cells, which was similar to the results shown in Fig. 3B. Furthermore, ROS generated by the 808 nm laser irradiated-ZnO-Ce6 NPs was approximately 1.5-fold higher than that by the 660 nm laser irradiated-Ce6 (Fig. 3F), suggesting that the ROS-generating function of 808 nm laser irradiated-ZnO-Ce6 NPs was stronger than that of 660 nm laser

irradiated-Ce6. In addition, the Ce6, ZnO NPs, 808 nm laser irradiated-ZnO NPs, and ZnO-Ce6 NPs generated very little or no ROS (Supporting Information Fig. S5).

The expression level of hypoxia-induced factor 1α (HIF-1α) in 4T1 cells under hypoxic (1% O_2) condition was measured using immunostaining after treatment with 808 nm laser irradiated-ZnO-Ce6 NPs and a strong HIF-1α signal (green) was detected in the control cells (Fig. 3G and H). Moreover, the HIF-1α level in the 4T1 cells after treatment with 660 nm laser irradiated-Ce6 was approximately 1.2 times higher than that in control 4T1 cells, owing to the aggravated oxygen-consuming procedure by PDT. However, the HIF-1α level after treatment with 808 nm laser irradiated-ZnO-Ce6 NPs was approximately 0.7 times lower than that in control, indicating that the hypoxia was alleviated because of oxygen supply. In addition, HIF-1α level significantly decreased after treatment with ZnO-Ce6 or 808 nm laser irradiated-ZnO NPs compared with that in control (Supporting Information Fig. S6), indicating that the hypoxia was alleviated because of oxygen supply by ZnO NP nanozymes.

The cellular ROS generation ability of ZnO-Ce6 NPs was evaluated under hypoxic conditions. The ROS levels after treatment with 808 nm laser irradiated-ZnO-Ce6 NPs and 660 nm laser irradiated-Ce6 were significantly higher than that in the control cells (approximately 5.9- and 1.9-times higher, respectively; Fig. 3I and J). Moreover, the ROS level after treatment with 808 nm laser irradiated-ZnO-Ce6 NPs group was 3.2-fold higher than that after treatment with 660 nm laser irradiated-Ce6, suggesting that the ROS-generating function of the 808 nm laser irradiated-ZnO-Ce6 NPs was significantly stronger than that of 660 nm laser irradiated-Ce6 under hypoxic conditions.

These results show that ZnO-Ce6 NPs generated oxygen in 4T1 cells because of the peroxidase-mimicking activity of ZnO NP nanozymes, which could supply oxygen to boost PDT and relieve hypoxia in tumor cells.

The cytotoxicity of the ROS produced by ZnO-Ce6 NPs on 4T1 cells was evaluated using the sulforhodamine B (SRB) method. The cytotoxicity of 808 nm laser irradiated-ZnO-Ce6 NPs was significantly enhanced than that of ZnO-Ce6 NPs (Supporting Information Fig. S7) since the 808 nm laser irradiated-ZnO-Ce6 NPs produced a considerable amount of ROS. In addition, the cytotoxicity of ZnO and ZnO-Ce6 NPs with or without the 808 nm laser was significantly enhanced compared to that of Ce6 due to the cytotoxicity of Zn^{2+}, which was further verified in Supporting Information Fig. S8.

Pearson's correlation coefficient was used to evaluate the co-localization of ZnO NPs and Ce6 after ZnO-Ce6 NPs entered the 4T1 cells. The Pearson correlation coefficient at the 1 h time point was 0.65 (Supporting Information Fig. S9), indicating that most ZnO-Ce6 NPs still maintained the combined structure of ZnO NPs and Ce6, which was conducive to ZnO NP emission to activate the neighboring Ce6.

3.3. *Overactivation of autophagy by ZnO-Ce6 NPs*

The overactivation of autophagy could be more efficient in avoiding cytoprotective functions and leading to cell death by triggering the autophagic cell death pathway[63,64]. We hypothesized that the ROS generated by 808 nm laser irradiated-ZnO-Ce6 NPs could overactivate autophagy, leading to tumor cell death[65]. Acidic cystic autophagosomes are produced during autophagy and can be detected using monodansyl cadaverine (MDC) staining. To examine autophagic flux after different treatments, we also determined the levels of LC3 and p62, two autophagy-related proteins. The blue fluorescence of acidic autophagosomes after treatment with 808 nm laser irradiated-ZnO-Ce6 NPs was considerably stronger than that after treatment with 660 nm laser irradiated-Ce6 (Fig. 4A). The level of LC3 protein after treatment with 808 nm laser irradiated-ZnO-Ce6 NPs was approximately 2.0-fold higher than that in the control cells and after treatment with 660 nm laser irradiated-Ce6 (Fig. 4B). Moreover, the green fluorescence of LC3 protein was significantly stronger after treatment with 808 nm laser irradiated-ZnO-Ce6 NPs than that after treatment with 660 nm laser irradiated-Ce6 (Fig. 4C and D). The ratio of LC3 II/LC3 I was increased, indicating that autophagy was overactivated (Fig. 4E and F). In addition, the level of p62 protein after treatment with 808 nm laser irradiated-ZnO-Ce6 NPs was higher than that in control (Fig. 4E−G, H, and Supporting Information Fig. S10), indicating hindered autophagosome degradation; moreover, excess accumulation of autophagosomes could cause cell death.

An annexin V/PI assay based on flow cytometry was performed to investigate the ZnO-Ce6 NP-induced cellular apoptosis. The apoptosis rate of 4T1 cells after treatment with 808 nm laser irradiated-ZnO-Ce6 NPs (91.81%) was significantly higher than that after treatment with 660 nm laser irradiated-Ce6 (74.42%, Fig. 4I and J). Therefore, the apoptosis of 4T1 cells was not inhibited by autophagy after treatment with 808 nm laser irradiated-ZnO-Ce6 NPs, further indicating that autophagy also contributed to the antitumor effect of 808 nm laser irradiated-ZnO-Ce6 NPs.

3.4. *Ferroptosis induced by ZnO-Ce6 NPs in the absence of laser irradiation*

ZnO-Ce6 NPs induce ferroptosis in tumor cells even in the absence of laser irradiation. Ferroptosis is a unique form of programmed cell death characterized by iron-dependent excess lipid peroxidation[66]. The lipid peroxidation levels after treatment with ZnO-Ce6 and ZnO NPs were significantly higher than that in the control (Fig. 5A). In addition, the ZnO-Ce6 and ZnO NPs increased the deep blue foci, indicating ferrous ion accumulation (Fig. 5I), which may be attributed to ZnO NPs modulating the uptake and export in iron homeostasis[67]. Ferroptosis is primarily controlled by the glutathione (GSH) redox system[68]. GSH depletion inactivates glutathione peroxidase 4 (GPX4), resulting in lipid peroxidation and subsequent ferroptosis [69,70]. ZnO and ZnO-Ce6 NPs significantly reduced GSH levels (Fig. 5B), GPX4 protein levels (Fig. 5C, D, and H), and GPX4 mRNA levels (Fig. 5E), which are typical features of ferroptosis. In the ferroptosis pathway, SLC7A11 is a transport subunit of the SLC7A11−GSH−GPX4 axis and an important cellular system for resistance to ferroptosis. SLC7A11 mRNA levels significantly decreased after treatment with ZnO-Ce6 and ZnO NPs (Fig. 5F). Arachidonate lipoxygenase (ALOX)-catalyzed lipid hydroperoxide generation promotes ferroptosis. ALOX15 mRNA levels significantly increased after treatment with ZnO-Ce6 and ZnO NPs (Fig. 5G), which may contribute to lipid peroxidation and ferroptosis. Illustration of the ferroptosis induced by ZnO-Ce6 NPs was shown in Fig. 5J.

3.5. *ICD induced by ZnO-Ce6 NPs in vitro*

PDT can cause ICD by inducing dying tumor cells to release immunogenic signals of DAMPs, including exposure to CRT on

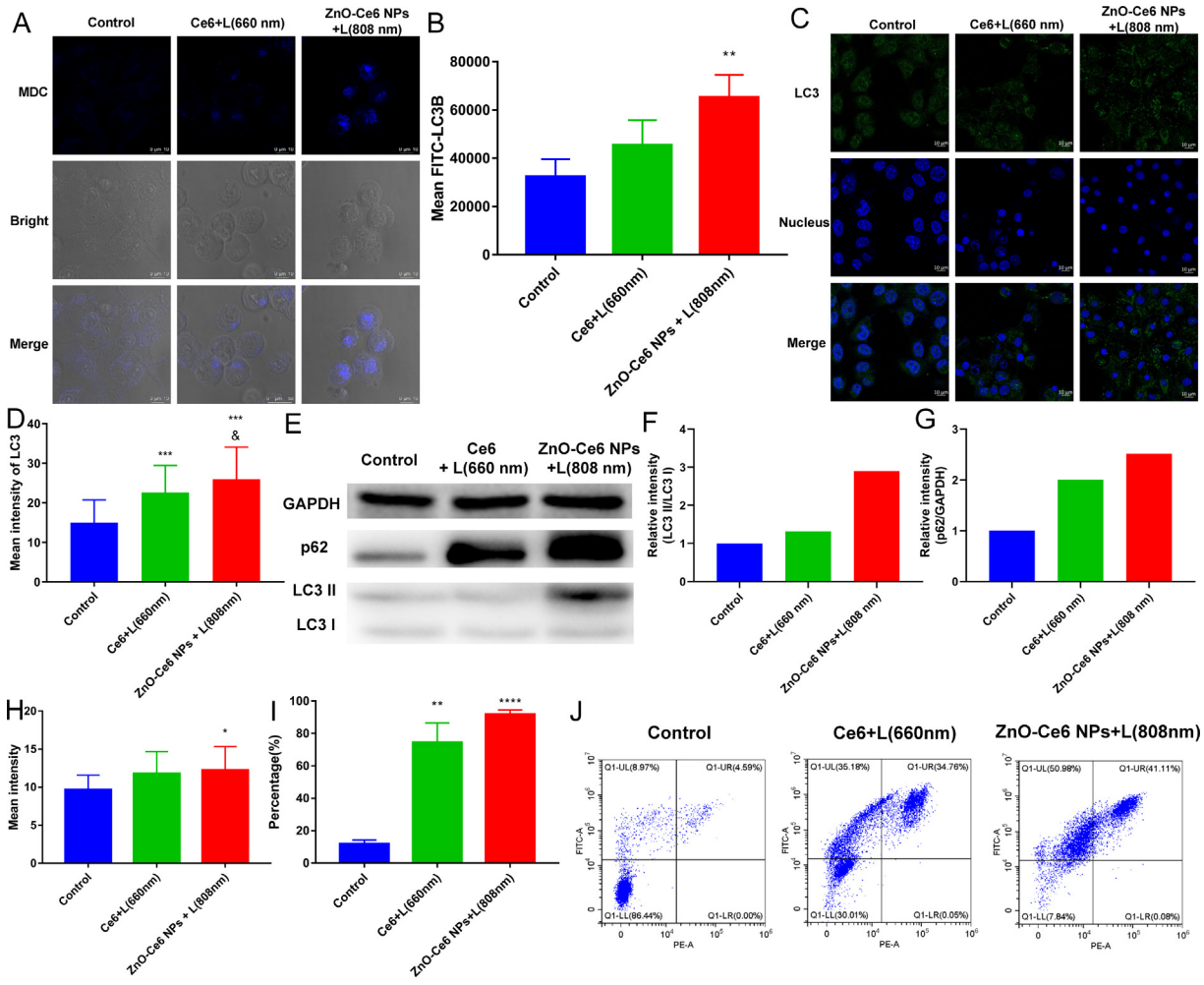

Figure 4 Overactivation of autophagy by 808 nm laser irradiated-ZnO-Ce6 NPs. (A) Monodansylcadaverine (MDC)-stained fluorescent images (scale bar = 10 μm); (B) Quantification of LC3 expression by flow cytometry; (C) Representative confocal images of LC3 protein in 4T1 cells after different treatments (scale bar = 10 μm); (D) Semi-quantitative analysis of LC3 protein; (E) Western blot analysis of LC3 and p62 protein; (F) Semi-quantitative analysis of LC3 II and LC3 I protein in Western blot; (G) Semi-quantitative analysis of p62 protein in Western blot; (H) Semi-quantitative analysis of p62 protein in immunofluorescence images; (I) Flow cytometry analysis of apoptotic cells after different treatments and (J) Representative scatter plots of apoptotic cells. Data are presented as mean ± SD ($n = 3$). *$P < 0.05$, **$P < 0.01$, ***$P < 0.001$, ****$P < 0.0001$ compared with the control; $^{\&}P < 0.05$ compared with 660 nm laser irradiated-Ce6 treatment.

the cell surface, ATP secretion, and HMGB1 release[71]. These signals promote DC maturation, which can effectively present antigens and mobilize host adaptive immunity. Since CRT, ATP, and HMGB1 are recognized as typical symbols of ICD, the *in vitro* ICD performance elicited by 808 nm laser irradiated-ZnO-Ce6 NPs was assessed in 4T1 cells.

CRT exposure on the 4T1 cell surface was investigated after treatment with 808 nm laser irradiated-ZnO-Ce6 NPs and further confirmed using flow cytometry (Fig. 6A and B). In addition, CRT exposure on the surface of 4T1 cells after treatment with 660 nm laser irradiated-Ce6 was significantly lower than that after treatment with 808 nm laser irradiated-ZnO-Ce6 NPs (Fig. 6B). Moreover, 808 nm laser irradiated-ZnO-Ce6 NP-induced HMGB1 and ATP release was significantly higher than that induced by 660 nm laser irradiated-Ce6 (Fig. 6C and D).

In addition, the *in vitro* results of BMDCs showed that the percentage of mature DCs promoted by DAMPs from 4T1 tumor cells after treatment with 808 nm laser irradiated-ZnO-Ce6 NPs was significantly higher than that in control and after treatment with 660 nm laser irradiated-Ce6, indicating that its role in inducing DC maturation was superior to that of 660 nm laser irradiated-Ce6 (Fig. 6E and F). The gating strategy used for the flow cytometry is shown in Supporting Information Fig. S11.

3.6. *Antitumor activity of ZnO-Ce6 NPs in vivo*

The *in vivo* antitumor activity of ZnO-Ce6 NPs was evaluated in 4T1-tumor-bearing BALB/c mice. Tumor growth was significantly inhibited after implanting 660 nm laser irradiated-Ce6 and 808 nm laser irradiated-ZnO-Ce6 NPs than that in control (Fig. 7A). However, the antitumor activity of 808 nm laser irradiated-ZnO-Ce6 NPs was significantly higher than that of 660 nm laser irradiated-Ce6. Notably, tumors were completely eradicated in three of the five 4T1-tumor-bearing mice on Day 27 after implanting 808 nm laser irradiated-ZnO-Ce6 NPs. Individual tumor growth curves are shown in Fig. 7B. The mean tumor size

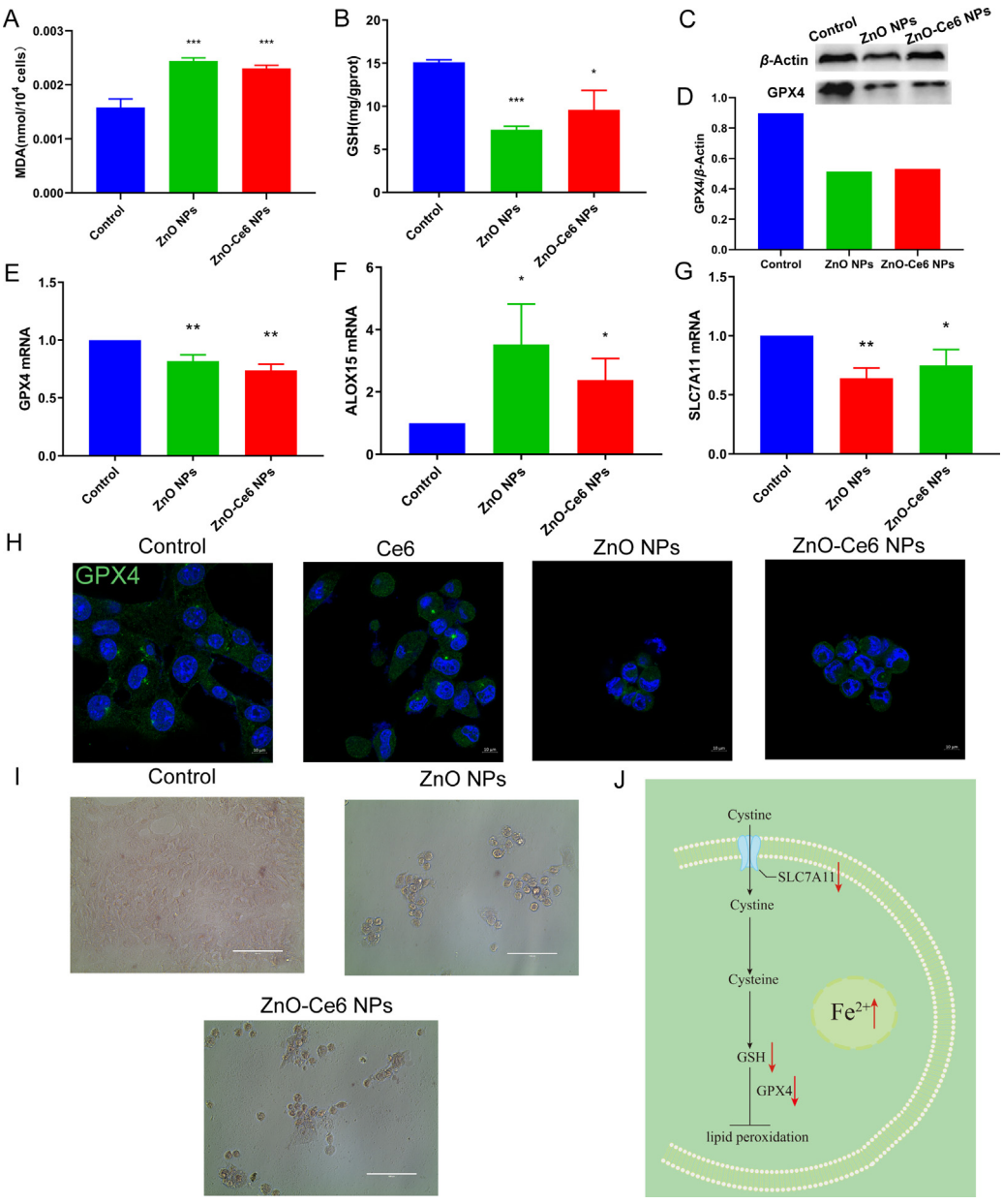

Figure 5 Ferroptosis induced by ZnO-Ce6 NPs in the absence of laser irradiation. (A) The level of lipid peroxidation; (B) Glutathione (GSH) levels detected by DTNB colorimetric assay; (C) GPX4 protein level analysis in 4T1 cells by Western blotting; (D) Semi-quantitative analysis of GPX4 protein by Western blotting; (E) Quantification of GPX4 mRNA levels by qPCR; (F) Quantification of SLC7A11 mRNA levels by qPCR; (G) Quantification of ALOX15 mRNA level by qPCR; (H) Representative immunofluorescence images of GPX4 protein in 4T1 cells (scale bar = 10 μm); (I) Optical micrographs of 4T1 cells stained with Lillie staining solution for divalent iron (blue, with pink nucleus counter-staining, scale bar = 100 μm); (J) Illustration of the ferroptosis induced by ZnO-Ce6 NPs. Data are presented as mean ± SD ($n = 3$). *$P < 0.05$, **$P < 0.01$, ***$P < 0.001$ compared with control.

on Day 27 in the control and after implanting 808 nm laser irradiated-ZnO-Ce6 NPs and 660 nm laser irradiated-Ce6 was 152 ± 208, 168 ± 131, and 1517 ± 123 mm^3, respectively. The corresponding tumor growth inhibition after implanting 808 nm laser irradiated-ZnO-Ce6 NPs and 660 nm laser irradiated-Ce6 was 90.0% and 80.2%, respectively, compared to that in the control. In addition, the antitumor activities of Ce6, 808 nm laser irradiated-Ce6, and ZnO-Ce6 NPs were negligible (Supporting Information Fig. S12). Moreover, the weight loss between the implanted and control groups was not substantial (Supporting Information Fig. S13).

The ROS level is a key factor in the antitumor activity of PDT. The *in vivo* ROS generation was investigated using a fluorescent probe (DCFH−DA). The ROS levels after implanting 808 nm laser irradiated-ZnO-Ce6 NPs and 660 nm laser irradiated-Ce6 were approximately 3.1- and 1.7-fold higher than that in the control, respectively (Fig. 7C and D). In addition, the ROS level after implanting 808 nm laser irradiated-ZnO-Ce6 NPs was approximately 1.8-fold higher than that after implanting 660 nm laser irradiated-Ce6, indicating that the PDT effect produced by 808 nm laser irradiated-ZnO-Ce6 NPs was stronger than that produced by 660 nm laser irradiated-Ce6 because ROS generation depends on

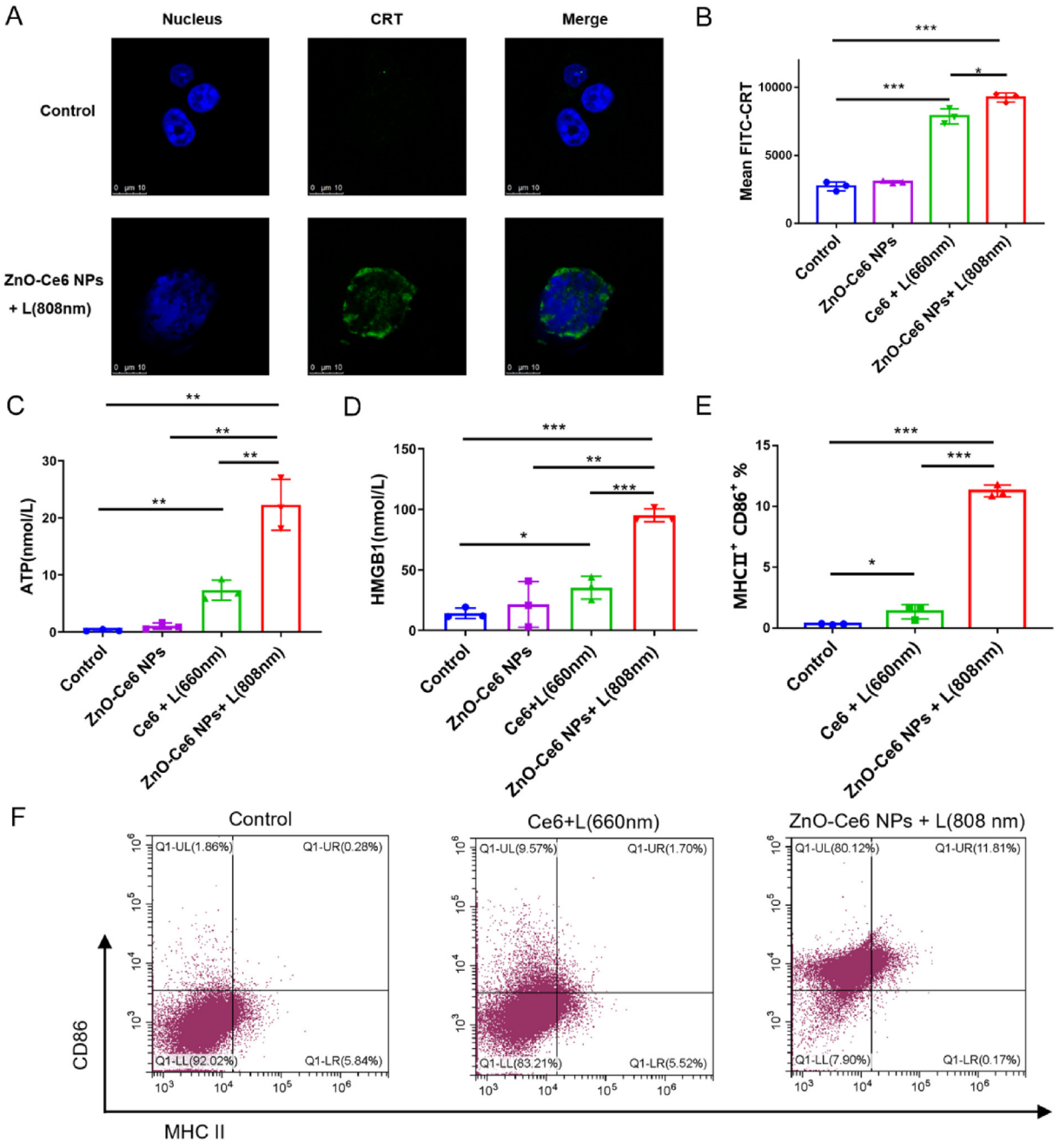

Figure 6 *In vitro* immunogenic cell death triggered by 808 nm laser irradiated-ZnO-Ce6 NPs. (A) CRT exposed on cells (scale bar = 10 μm); (B) Quantification of CRT exposed on cells by flow cytometry; (C) Analysis of ATP secretion; (D) Analysis of HMGB1 release; (E) Analysis of dendritic cell (DC) maturation by flow cytometry after incubating with the 4T1 cell supernatant; (F) Representative scatter plots of mature DCs. Data are presented as mean ± SD ($n = 3$). *$P < 0.05$, **$P < 0.01$, ***$P < 0.001$.

oxygen supply. ZnO-Ce6 NPs comprise ZnO NP nanozymes with a peroxidase-mimicking activity that produces oxygen for further oxygen supply in PDT. Therefore, the ROS generation was enhanced after implanting 808 nm laser irradiated-ZnO-Ce6 NPs. However, ROS generation after implanting 808 nm laser irradiated-Ce6 was severely impaired due to limited oxygen supply.

Tumor tissues generally suffer from severe hypoxia, which significantly affects PDT efficiency. Moreover, oxygen-consuming PDT aggravates hypoxia and reduces efficacy. Since ZnO NP nanozymes can supply oxygen, the effect of ZnO-Ce6 NPs against tumor hypoxia was investigated using fluorescent-tagged antibodies binding to endogenous HIF-1α and CD31 on blood vessels. Typically, both HIF-1α and CD31 downregulation indicate relief from hypoxia in solid tumors.

Large areas of HIF-1α (green) and CD31 (red) signals were observed in control, indicating the extensively distributed hypoxic areas in tumor tissues (Fig. 7E and F). The HIF-1α level after implanting 660 nm laser irradiated-Ce6 increased compared with that in the control, suggesting the hypoxia aggravated in tumors. However, HIF-1α and CD31 levels after implanting 808 nm laser irradiated-ZnO-Ce6 NPs decreased significantly compared with that in control and after implanting 660 nm laser irradiated-Ce6,

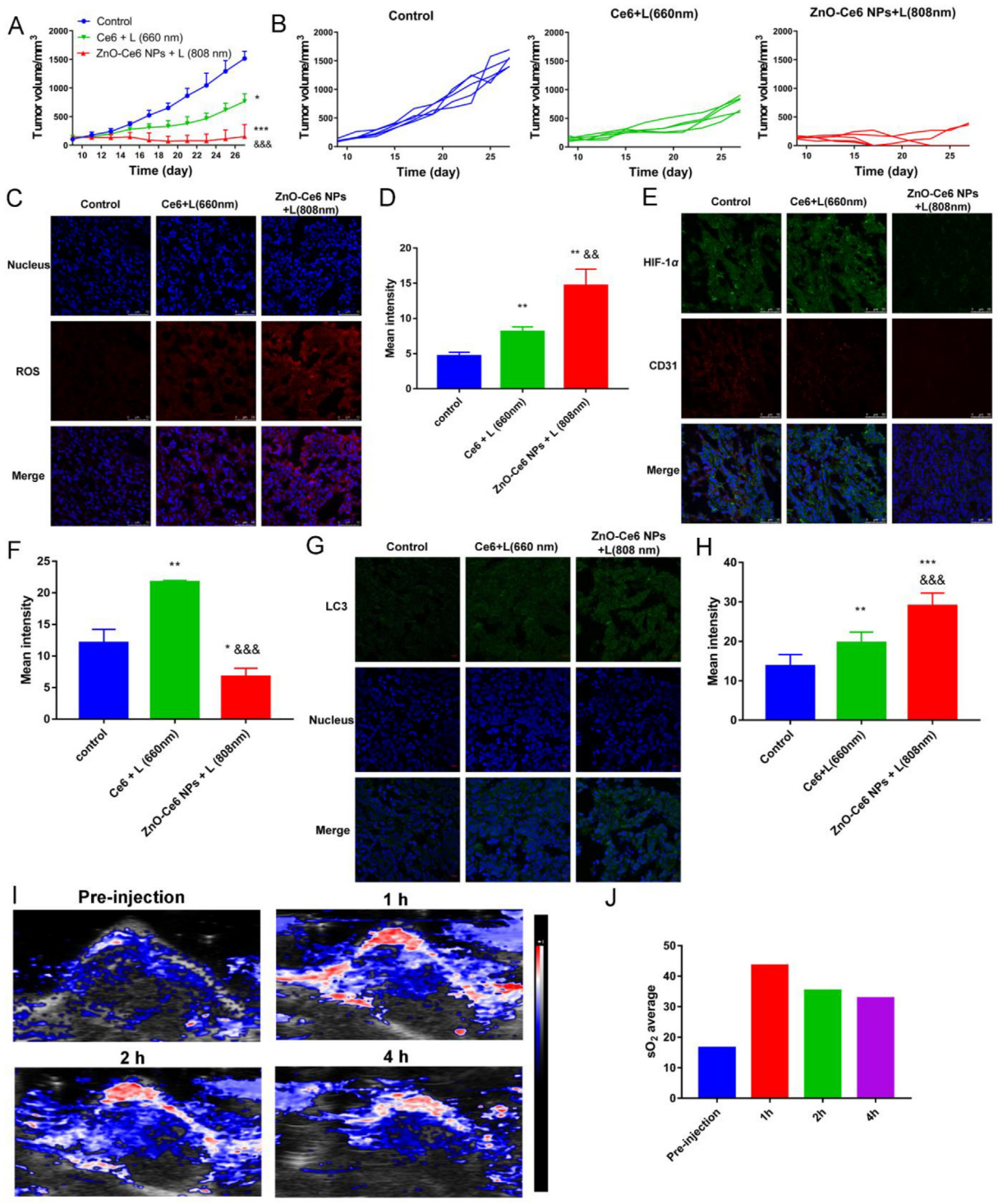

Figure 7 *In vivo* antitumor activity of ZnO-Ce6 NPs. (A) The tumor growth curves of 4T1-tumor-bearing BALB/c mice ($n = 5$); (B) Individual tumor growth curve of 4T1-tumor-bearing BALB/c mice; (C) ROS immunofluorescence in tumor sections (scale bar = 50 μm) and (D) Semi-quantitative analysis of ROS ($n = 3$); (E) HIF-1α and CD31 immunofluorescence in tumor sections (scale bar = 50 μm) and (F) Semi-quantitative analysis of HIF-1α ($n = 3$); (G) LC3 immunofluorescence in tumor sections (scale bar = 10 μm) and (H) Semi-quantitative analysis of LC3 ($n = 3$); (I) Photoacoustic imaging showing sO_2 levels in tumors after injecting ZnO-Ce6 NPs at different time-points, and (J) Semi-quantitative analysis of sO_2 average. Data are presented as mean ± SD. $^{*}P < 0.05$, $^{**}P < 0.01$, $^{***}P < 0.001$ compared with control; $^{\&\&}P < 0.01$, $^{\&\&\&}P < 0.001$ compared with 660 nm laser irradiated-Ce6 treatment.

indicating that the hypoxia in tumor tissues was alleviated due to ZnO NP nanozymes with peroxidase−mimic activity. Furthermore, the HIF-1α level after implanting 660 nm laser irradiated-Ce6 and 808 nm laser irradiated-ZnO-Ce6 NPs were about 1.8-fold higher and 0.56-times lower, respectively, than that of the control (Fig. 7D). In addition, 808 nm laser irradiated-ZnO NPs

alleviated tumor hypoxia as ZnO NP nanozymes convert hydrogen peroxide into oxygen (Supporting Information Fig. S14).

To directly verify the oxygen levels in tumors, photoacoustic imaging was performed to monitor the oxygen content in the tumor tissues of 4T1-tumor-bearing mice by measuring tumor vascular-saturated O_2 (sO_2) at two excitation wavelengths (750 and 850 nm). Vascular oxygen saturation was assessed by observing the hemoglobin (Hb) and oxyhemoglobin (HbO_2) signal intensities in the tumor blood (blue and red, respectively). When the oxygen content decreased, the HbO_2 content decreased, and the red signal weakened. The sO_2 before the implantation was 16.5% (Fig. 7I and J). The red signal amplified 1 h post-injection. The sO_2 1 and 4 h post-injection were 43.5% and 32.8%, respectively, which were 2.6 and 2.0 times higher, respectively, than those before injection. These results directly indicate oxygen generation and relief from hypoxia.

To study the cellular autophagic flux in the tumor tissue, the level of autophagy-related protein LC3 was determined. The LC3 level after implanting 808 nm laser irradiated-ZnO-Ce6 NPs was 2.1 and 1.5 times higher than that in control and after implanting

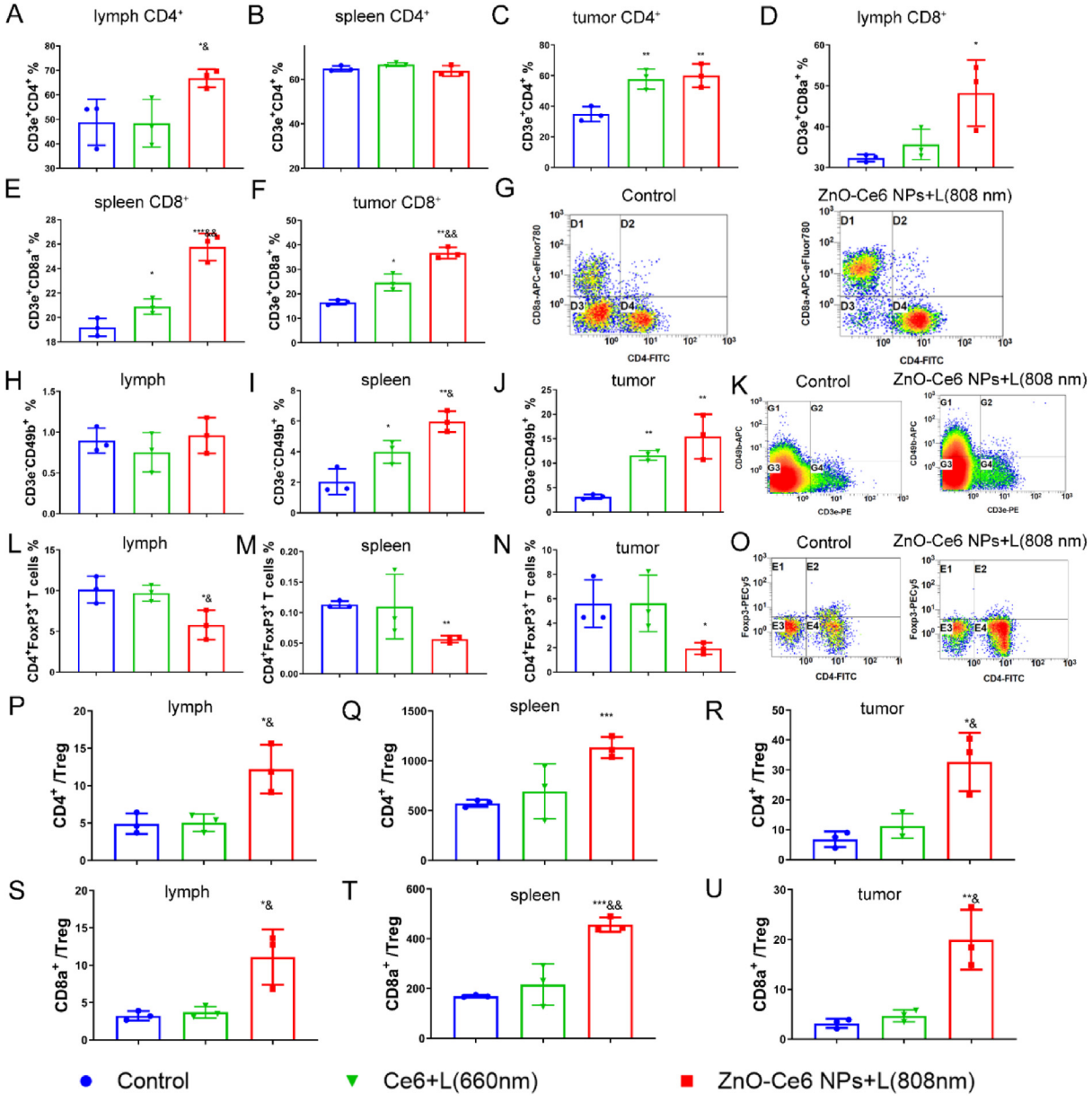

Figure 8 *In vivo* immune responses. (A−F) Flow cytometric analysis of $CD4^+$ and $CD8^+$ T cells in tumor -draining lymph nodes, spleens, and tumors, and (G) Representative scatter plots of $CD4^+$ and $CD8^+$ T cells in tumors; (H−J) Flow cytometric analysis of natural killer (NK) cells in tumor-draining lymph nodes, spleens, and tumors, and (K) Representative scatter plots of NK cells in tumors; (L−N) Flow cytometric analysis of regulatory T cells (Tregs) in tumor-draining lymph nodes, spleens, and tumors, and (O) Representative scatter plots of Tregs in tumors; (P, R) $CD4^+$/Treg ratio in tumor-draining lymph nodes, spleens, and tumors; (S−U) $CD8^+$/Treg ratio in tumor-draining lymph nodes, spleens, and tumors. Data are presented as mean ± SD ($n = 3$). $^*P < 0.05$, $^{**}P < 0.01$, $^{***}P < 0.001$ compared with control; $^{\&}P < 0.05$, $^{\&\&}P < 0.01$, $^{\&\&\&}P < 0.001$ compared with 660 nm laser irradiated-Ce6 treatment.

660 nm laser irradiated-Ce6, respectively (Fig. 7G and H), indicating that overactivation of autophagy in the tumor was induced by 808 nm laser irradiated-ZnO-Ce6 NPs, which could contribute to killing tumor cells.

3.7. *Systemic immunity induced by ZnO-Ce6 NPs in vivo*

The ICD markers were investigated *in vivo*. The 808 nm laser irradiated-ZnO-Ce6 NPs elicited CRT exposure and HMGB1 release *in vivo* (Supporting Information Figs. S15 and S16), similar to the *in vitro* results, which indicated that PDT induced by 808 nm laser irradiated-ZnO-Ce6 NPs elicited ICD *in vivo*.

The ability to promote DC maturation and T cell activation through ICD signaling molecules was assessed.

As shown in Supporting Information Fig. S17, mature DCs in the tumor-draining lymph nodes and spleen greatly increased after implanting 808 nm laser irradiated-ZnO-Ce6 NPs compared to those in the control mice. Flow cytometry analysis indicated that mature DCs in tumors also significantly increased after implanting 808 nm laser irradiated-ZnO-Ce6 NPs compared to that in the control, which was also verified in the immunofluorescence images of tumor sections (Supporting Information Fig. S18). The gating strategy for flow cytometry to detect mature DCs *in vivo* is shown in Supporting Information Fig. S19.

Mature DCs play a vital role in initiating an effective adaptive immune response by presenting antigens to the T lymphocytes for further antitumor effect[72,73]. Therefore, the proportion of T lymphocytes (such as $CD4^+$ T cells, $CD8^+$ T cells, and Tregs) and NK cells in the tumor-draining lymph nodes, spleen, and tumors were further investigated.

The proportion of activated $CD8^+$ T cells, $CD4^+$ T cells, and NK cells in tumors; activated $CD4^+$ T cells in tumor-draining lymph nodes; $CD8^+$ T cells in tumor-draining lymph nodes and spleen; and NK cells in the spleen significantly increased after treatment with 808 nm laser irradiated-ZnO-Ce6 NPs than those in control (Fig. 8A−K), indicating that these immune cells possessed strong antitumor immunity effects for effectively killing tumor cells *in vivo*. Treatment with 808 nm laser irradiated-ZnO-Ce6 NPs significantly reduced the proportion of Tregs in the tumor-draining lymph nodes, spleen, and tumors compared to that in the control (Fig. 8L−O), indicating that treatment with 808 nm laser irradiated-ZnO-Ce6 NPs could alleviate immunosuppression. The immunofluorescence images of the tumor sections were similar to those obtained by flow cytometry (Supporting Information Figs. S20 and S21).

The $CD4^+$/Treg and $CD8^+$/Treg ratios after treatment with 808 nm laser irradiated-ZnO-Ce6 NPs significantly increased in tumor-draining lymph nodes, spleen, and tumors compared to those in the control group (Fig. 8P−U).

In addition, 660 nm laser irradiated-Ce6 also increased the proportion of $CD4^+$ T cells in the tumors, as well as $CD8^+$ T and NK cells in the spleen and tumors; however, they were still lower than that after treatment with 808 nm laser irradiated-ZnO-Ce6 NPs. The gating strategy for flow cytometry to detect $CD4^+$ T cells, $CD8^+$ T cells, NK cells, and Tregs is shown in Supporting Information Fig. S22.

The results indicated that ICD induced by 808 nm laser irradiated-ZnO-Ce6 NPs further stimulated immune responses, including $CD4^+$ and $CD8^+$ T cell proliferation, NK cell upregulation, and Treg downregulation, *via* DC maturation, which enhanced the antitumor effect of PDT in 4T1-tumor-bearing BALB/c mice.

4. Conclusions

We prepared biocompatible and environment-friendly ZnO NPs and evaluated their upconversion properties and catalase-like nanozyme activity. Accordingly, we used ZnO NPs to prepare multifunctional ZnO-Ce6 NPs, which simultaneously resolve the issues of poor penetration and hypoxia for PDT. Compared with free Ce6 requiring 660 nm visible light excitation, ZnO-Ce6 NPs converted 808 nm NIR light to 401 nm light to excite Ce6, which improved penetration by extending the wavelength to the NIR region. Owing to the peroxidase-mimicking activity of ZnO NP nanozymes, ZnO-Ce6 NPs can supply oxygen to boost PDT and relieve hypoxia in tumors. The enhanced photodynamic action, overactivation of pro-death autophagy, ICD of tumor cells, and activated systemic immunity exert antitumor effects after addressing these limitations. In addition, ZnO-Ce6 NPs induced ferroptosis in tumors even in the absence of laser irradiation. The *in vitro* and *in vivo* results indicated that ZnO-Ce6 NPs significantly inhibited tumor growth and completely eradicated individual tumors, which are expected to solve penetration and hypoxia problems associated with PDT in clinical applications. Owing to their optical properties, nanozyme functions, and biological effects such as ferroptosis, ZnO NPs are promising carriers for other drugs to establish nanoplatforms and construct various multifunctional nano-drug deliveries.

Authors contribution

Jingru Wang: Investigation. Man Liu: Investigation. ingwen Wang: Investigation. Zhuoyue Li: Investigation. Zhenhan Feng: Investigation. Meiqi Xu: Investigation. Hui Wang: Investigation. Hui Li: Investigation. Zhantao Li: Investigation. Jianming Yu: Investigation. Junwei Liu: Investigation. Qingchao Wei: Investigation. Shuang Zhang: Investigation. Xuan Zhang: Writing − review & editing.

Conflicts of interest

The authors have no conflicts of interest to declare.

Acknowledgments

Authors gratefully acknowledge the financial support from the National Natural Science Foundation of China (No. 81773646), the National Key Research and Development Program of China (2017YFA0205600), and the Innovation Team of the Ministry of Education (No. BMU2017TD003, China).

Appendix A. Supporting information

Supporting information to this article can be found online at https://doi.org/10.1016/j.apsb.2024.07.002.

References

1. Peña Q, Wang A, Zaremba O, Shi Y, Scheeren HW, Metselaar JM, et al. Metallodrugs in cancer nanomedicine. *Chem Soc Rev* 2022;**51**:2544−82.
2. Xia DL, Hang DM, Li YY, Jiang W, Zhu JF, Ding Y, et al. Au−hemoglobin loaded platelet alleviating tumor hypoxia and enhancing the radiotherapy effect with low-dose X-ray. *ACS Nano* 2020;**14**:15654−68.

3. Dykman LA, Khlebtsov NG. Multifunctional gold-based nanocomposites for theranostics. *Biomaterials* 2016;**108**:13−34.
4. Deng RH, Zou MZ, Zheng DW, Peng SY, Liu WL, Bai XF, et al. Nanoparticles from cuttlefish ink inhibit tumor growth by synergizing immunotherapy and photothermal therapy. *ACS Nano* 2019;**13**:8618−29.
5. Ho E, Wong CP, King JC. Impact of zinc on DNA integrity and age-related inflammation. *Free Radic Biol Med* 2022;**178**:391−7.
6. Djurisic AB, Leung YH. Optical properties of ZnO nanostructures. *Small* 2006;**2**:944−61.
7. Lei ZD, Ling X, Mei QS, Fu S, Zhang J, Zhang Y. An excitation navigating energy migration of lanthanide ions in upconversion nanoparticles. *Adv Mater* 2020;**32**:1906225.
8. Zhao MY, Zhuang HJ, Li BH, Chen MW, Chen XY. In situ transformable nanoplatforms with supramolecular cross-linking triggered complementary function for enhanced cancer photodynamic therapy. *Adv Mater* 2023;**35**:2209944.
9. Comotti M, Pina CD, Matarrese R, Rossi M. The catalytic activity of "naked" gold particles. *Angew Chem Int Ed Engl* 2004;**43**:5812−5.
10. Zhang Y, Wang FM, Liu CQ, Wang ZZ, Kang LH, Huang YY, et al. Nanozyme decorated metal-organic frameworks for enhanced photodynamic therapy. *ACS Nano* 2018;**12**:651−61.
11. Wei H, Wang E. Nanomaterials with enzyme-like characteristics (nanozymes): next-generation artificial enzymes. *Chem Soc Rev* 2013;**42**:6060−93.
12. Su WY, Huang JS, Lin CF. Improving the property of ZnO nanorods using hydrogen peroxide solution. *J Cryst Growth* 2008;**310**:2806−9.
13. Agostinis P, Berg K, Cengel KA, Foster TH, Girotti AW, Gollnick SO, et al. Photodynamic therapy of cancer: an update. *CA Cancer J Clin* 2011;**61**:250−81.
14. Chen JM, Fan TJ, Xie ZJ, Zeng QQ, Xue P, Zheng TT, et al. Advances in nanomaterials for photodynamic therapy applications: status and challenges. *Biomaterials* 2020;**237**:119827.
15. Dolmans DE, Fukumura D, Jain RK. Photodynamic therapy for cancer. *Nat Rev Cancer* 2003;**3**:380−7.
16. Phua SZF, Yang GB, Lim WQ, Verma A, Chen HZ, Thanabalu T, et al. Catalase-integrated hyaluronic acid as nanocarriers for enhanced photodynamic therapy in solid tumor. *ACS Nano* 2019;**13**:4742−51.
17. Li XS, Lee SY, Yoon JY. Supramolecular photosensitizers rejuvenate photodynamic therapy. *Chem Soc Rev* 2018;**47**:1174−88.
18. Straten DV, Mashayekhi V, Bruijn HSD, Oliveira S, Robinson DJ. Oncologic photodynamic therapy: basic principles, current clinical status and future directions. *Cancers (Basel)* 2017;**9**:19.
19. Lucky SS, Soo CK, Zhang Y. Nanoparticles in photodynamic therapy. *Chem Rev* 2015;**115**:1990−2042.
20. Lu KD, He CB, Lin WB. Nanoscale metal-organic framework for highly effective photodynamic therapy of resistant head and neck cancer. *J Am Chem Soc* 2014;**136**:16712−5.
21. Reiners JJ, Agostinis P, Berg K, Oleinick NL, Kessel DH. Assessing autophagy in the context of photodynamic therapy. *Autophagy* 2010;**6**:7−18.
22. Dewaele M, Maes H, Agostinis. ROS-mediated mechanisms of autophagy stimulation and their relevance in cancer therapy. *Autophagy* 2010;**6**:838−54.
23. Ding ZB, Hui B, Shi YH, Zhou J, Peng YF, Gu CY, et al. Autophagy activation in hepatocellular carcinoma contributes to the tolerance of oxaliplatin *via* reactive oxygen species modulation. *Clin Cancer Res* 2011;**17**:6229−38.
24. Galluzzi L, Vitale I, Aaronson SA, Abrams JM, Adam D, Agostinis P, et al. Molecular mechanisms of cell death: recommendations of the nomenclature committee on cell death 2018. *Cell Death Differ* 2018;**25**:486−541.
25. Mroz P, Hashmi JT, Huang YY, Lange N, Hamblin MR. Stimulation of antitumor immunity by photodynamic therapy. *Expert Rev Clin Immunol* 2011;**7**:75−91.
26. Castano AP, Mroz P, Hamblin MR. Photodynamic therapy and anti-tumour immunity. *Nat Rev Cancer* 2006;**6**:535−45.
27. Luo L, Zhang Q, Luo YH, He ZG, Tian XH, Battaglia G, et al. Thermosensitive nanocomposite gel for intra-tumoral two-photon photodynamic therapy. *J Control Release* 2019;**298**:99−109.
28. Tian G, Gu ZG, Zhou LJ, Yin WY, Liu XX, Yan L, et al. Mn^{2+} dopant-controlled synthesis of $NaYF_4$:Yb/Er upconversion nanoparticles for *in vivo* imaging and drug delivery. *Adv Mater* 2012;**24**:1226−31.
29. Shcherbo D, Merzlyak EM, Chepurnykh TV, Fradkov AF, Ermakova GV, Solovieva EA, et al. Bright far-red fluorescent protein for whole-body imaging. *Nat Methods* 2007;**4**:741−6.
30. Liu HL, Yang Y, Wang AH, Han MJ, Cui W, Li JB. Hyperbranched polyglycerol-doped mesoporous silica nanoparticles for one- and two-photon activated photodynamic therapy. *Adv Funct Mater* 2016;**26**:2561−70.
31. Chou KL, Won N, Kwag J, Kim S, Chen JY. Femto-second laser beam with a low power density achieved a two-photon photodynamic cancer therapy with quantum dots. *J Mater Chem B* 2013;**1**:4584−92.
32. Xu J, Xu LG, Wang CY, Yang R, Zhuang Q, Han X, et al. Near-infrared-triggered photodynamic therapy with multitasking upconversion nanoparticles in combination with checkpoint blockade for immunotherapy of colorectal cancer. *ACS Nano* 2017;**11**:4463−74.
33. Cai HJ, Shen TT, Zhang J, Shan CF, Jia JG, Li X, et al. A core-shell metal-organic-framework (MOF)-based smart nanocomposite for efficient NIR/H_2O_2-responsive photodynamic therapy against hypoxic tumor cells. *J Mater Chem B* 2017;**5**:2390−4.
34. Fan WP, Huang P, Chen XY. Overcoming the Achilles' heel of photodynamic therapy. *Chem Soc Rev* 2016;**45**:6488−519.
35. Li XS, Kwon NY, Guo T, Liu Z, Yoon JY. Innovative strategies for hypoxic-tumor photodynamic therapy. *Angew Chem Int Ed Engl* 2018;**57**:11522−31.
36. Luo ZY, Zheng MB, Zhao PF, Chen Z, Siu FM, Gong P, et al. Self-monitoring artificial red cells with sufficient oxygen supply for enhanced photodynamic therapy. *Sci Rep* 2016;**6**:23393.
37. Wang JP, Liu L, You Q, Song YL, Sun Q, Wang YD, et al. All-in-one theranostic nanoplatform based on hollow mosx for photothermally-maneuvered oxygen self-enriched photodynamic therapy. *Theranostics* 2018;**8**:955−71.
38. Day RA, Estabrook DA, Logan JK, Sletten EM. Fluorous photosensitizers enhance photodynamic therapy with perfluorocarbon nanoemulsions. *Chem Commun* 2017;**53**:13043−6.
39. Yang GB, Xu LG, Xu J, Zhang R, Song GS, Chao Y, et al. Smart nanoreactors for pH-responsive tumor homing, mitochondria-targeting, and enhanced photodynamic-immunotherapy of cancer. *Nano Lett* 2018;**18**:2475−84.
40. Lin TS, Zhao XZ, Zhao S, Yu H, Cao WM, Chen W, et al. O_2-generating MnO_2 nanoparticles for enhanced photodynamic therapy of bladder cancer by ameliorating hypoxia. *Theranostics* 2018;**8**:990−1004.
41. Zhang CP, Liu ZX, Zhang YH, Ma L, Song EQ, Song Y, et al. "Iron free" zinc oxide nanoparticles with ion-leaking properties disrupt intracellular ROS and iron homeostasis to induce ferroptosis. *Cell Death Dis* 2020;**11**:183.
42. Li ZY, Zhang S, Liu M, Zhong T, Li H, Wang JR, et al. Antitumor activity of the zinc oxide nanoparticles coated with low-molecular-weight heparin and doxorubicin complex *in vitro* and *in vivo*. *Mol Pharm* 2022;**19**:4179−90.
43. Zhang SQ, Li YH, Li ZY, Wang GX, Liao A, Wang JR, et al. Intelligent nanodelivery system-generated $^1O_2$ mediates tumor vessel normalization by activating endothelial TRPV4-eNOS signaling. *Small* 2022;**18**:2200038.
44. Li ZY, Wang JR, Liu JW, Yu JM, Wang JW, Wang H, et al. Multifunctional ZnO@DOX/ICG-LMHP nanoparticles for synergistic multimodal antitumor activity. *J Funct Biomater* 2024;**15**:35.
45. Zhang S, Li ZT, Liu M, Wang JR, Xu MQ, Li ZY, et al. Anti-tumour activity of low molecular weight heparin doxorubicin nanoparticles for histone H1 high-expressive prostate cancer PC-3M cells. *J Control Release* 2019;**295**:102−17.
46. Feng ZH, Li ZT, Zhang S, Wang JR, Li ZY, Xu MQ, et al. A combination strategy based on an au nanorod/doxorubicin gel *via* mild photothermal therapy combined with antigen-capturing liposomes and

anti-PD-L1 agent promote a positive shift in the cancer-immunity cycle. *Acta Biomater* 2021;**136**:495−507.
47. Hu X, Tian HL, Jiang W, Song AX, Li ZH, Luan YX. Rational design of IR820- and ce6-based versatile micelle for single NIR laser−induced imaging and dual-modal phototherapy. *Small* 2018;**14**:1802994.
48. Wang JR, Zhang S, Li ZY, Xu MQ, Wang GX, Zhang X. Preparation and characterization of ph-sensitive calcium carbonate-chlorin e6 nanoparticles for photodynamic therapy. *J Chin Pharmaceut Sci* 2021;**30**:904−11.
49. Chen Y, Zhao J, Yu YL, Liu XY, Lin L, Zhang FM, et al. Antithrombin iii-binding site analysis of low-molecular-weight heparin fractions. *J Pharm Sci* 2018;**107**:1290−5.
50. Qiao JN, Liu SH, Huang YF, Zhu X, Xue CY, Wang Y, et al. Glycolysis-non-canonical glutamine dual-metabolism regulation nanodrug enhanced the phototherapy effect for pancreatic ductal adenocarcinoma treatment. *J Colloid Interf Sci* 2024;**665**:477−90.
51. Du S, Yu Y, Xu C, Xiong H, Yang S, Yao J. LMWH and its derivatives represent new rational for cancer therapy: construction strategies and combination therapy. *Drug Discov Today* 2019;**24**:2096−104.
52. Zhang J, Shin MC, David AE, Zhou J, Lee K, He HN, et al. Long-circulating heparin-functionalized magnetic nanoparticles for potential application as a protein drug delivery platform. *Mol Pharm* 2013;**10**:3892−902.
53. Ma SN, Mao ZX, Wu Y, Liang MX, Wang DD, Chen X, et al. The anti-cancer properties of heparin and its derivatives: a review and prospect. *Cell Adhes Migr* 2020;**14**:118−28.
54. Bae KH, Mok H, Park TG. Synthesis, characterization, and intracellular delivery of reducible heparin nanogels for apoptotic cell death. *Biomaterials* 2008;**29**:3376−83.
55. Huang JX, Zhuang C, Chen J, Chen XM, Li XJ, Zhang T, et al. Targeted drug/gene/photodynamic therapy *via* a stimuli-responsive dendritic-polymer-based nanococktail for treatment of EGFR-TKI-resistant non-small-cell lung cancer. *Adv Mater* 2022;**34**:2201516.
56. Zhu LW, You YC, Zhu MX, Song YL, Zhang JC, Hu JH, et al. Ferritin-hijacking nanoparticles spatiotemporally directing endogenous ferroptosis for synergistic anticancer therapy. *Adv Mater* 2022;**34**:2207174.
57. Wan YL, Fu LH, Li CY, Lin J, Huang P. Conquering the hypoxia limitation for photodynamic therapy. *Adv Mater* 2021;**33**:2103978.
58. Liu JN, Bu WB, Shi JL. Chemical design and synthesis of functionalized probes for imaging and treating tumor hypoxia. *Chem Rev* 2017;**117**:6160−224.
59. Wu TT, Liu Y, Cao Y, Liu ZH. Engineering macrophage exosome disguised biodegradable nanoplatform for enhanced sonodynamic therapy of glioblastoma. *Adv Mater* 2022;**34**:2110364.
60. Song GS, Chen YY, Liang C, Yi X, Liu JJ, Sun XQ, et al. Catalase-loaded taox nanoshells as bio-nanoreactors combining high-Z element and enzyme delivery for enhancing radiotherapy. *Adv Mater* 2016;**28**:7143−8.
61. Wang J, Xu MZ, Zhao RR, Chen GN. A highly sensitive H_2O_2 sensor based on zinc oxide nanorod arrays film sensing interface. *Analyst* 2010;**135**:1992−6.
62. Altunbek M, Baysal A, Çulha M. Influence of surface properties of zinc oxide nanoparticles on their cytotoxicity. *Colloids Surf B Biointerfaces* 2014;**121**:106−13.
63. Deng YY, Song PY, Chen XH, Huang Y, Hong LJ, Jin Q, et al. 3-Bromopyruvate-conjugated nanoplatform-induced pro-death autophagy for enhanced photodynamic therapy against hypoxic tumor. *ACS Nano* 2020;**14**:9711−27.
64. Maiuri MC, Zalckvar E, Kimchi A, Kroemer G. Self-eating and self-killing: crosstalk between autophagy and apoptosis. *Nat Rev Mol Cel Biol* 2007;**8**:741−52.
65. Wang T, Hu JH, Luo H, Li HY, Zhou JH, Zhou L, et al. Photosensitizer and autophagy promoter coloaded ROS-responsive dendrimer-assembled carrier for synergistic enhancement of tumor growth suppression. *Small* 2018;**14**:1802337.
66. Chen CA, Wang DK, Yu YY, Zhao TY, Min NN, Wu Y, et al. Legumain promotes tubular ferroptosis by facilitating chaperone-mediated autophagy of GPX4 in aki. *Cel Death Dis* 2021;**12**:65.
67. Zhang CP, Liu ZX, Zhang YH, Ma L, Song EQ, Song Y. "Iron free" zinc oxide nanoparticles with ion-leaking properties disrupt intracellular ROS and iron homeostasis to induce ferroptosis. *Cel Death Dis* 2020;**11**:183.
68. Gao WT, Wang XY, Zhou Y, Wang XQ, Yu Y. Autophagy, ferroptosis, pyroptosis, and necroptosis in tumor immunotherapy. *Signal Transduction Targeted Ther* 2022;**7**:196.
69. Lei G, Zhuang L, Gan BY. Targeting ferroptosis as a vulnerability in cancer. *Nat Rev Cancer* 2022;**22**:381−96.
70. Liang DG, Minikes AM, Jiang XJ. Ferroptosis at the intersection of lipid metabolism and cellular signaling. *Mol Cel* 2022;**82**:2215−27.
71. Alzeibak R, Mishchenko TA, Shilyagina NY, Balalaeva IV, Vedunova MV, Krysko DV. Targeting immunogenic cancer cell death by photodynamic therapy: past, present and future. *J Immunother Cancer* 2021;**9**:e001926.
72. He SQ, Wang LL, Wu DX, Tong F, Zhao H, Li HM, et al. Dual-responsive supramolecular photodynamic nanomedicine with activatable immunomodulation for enhanced antitumor therapy. *Acta Pharm Sin B* 2024;**14**:765−80.
73. Choi Y, Son W, Han YP, Chae JY, Yang CS, Choi JH. Glycan targeting nanoparticle for photodynamic immunotherapy of melanoma. *Acta Pharm Sin B* 2023;**13**:1903−18.